JOURNAL OF MATERIALS SCIENCE 33 (1998) 4389–4400

# Effect of martensitic transformation in Ti–15 at% V β-phase particles on lamellar boundary decohesion in γ-TiAl

## Part I *Derivation of interface decohesion potentials*

M. GRUJICIC, S. G. LAI
*Program in Materials Science and Engineering, Department of Mechanical Engineering, 241 Flour Daniel Building, Clemson University, Clemson, SC 29634–0921, USA*

Molecular statics atomistic simulations of the Ti–15 at% V body-centred cubic (bcc) β-phase–γ-TiAl interface and γ–γ lamellar boundary decohesion processes have been carried out to determine the corresponding decohesion potentials. The potentials are subsequently related to the dislocation structure of the interface–boundary. Atomic interactions have been represented using the appropriate embedded atom method (EAM) interatomic potential functions. The results obtained show that the decohesion potential functions are quite complex because they have to account for the instabilities that occur under some modes of interface decohesion and for the periodic character of the interfacial shear. Lastly, the use of decohesion potentials to derive constitutive relations for continuum-type interfacial elements and their implementation in the finite element method are presented.


## 1. Introduction

γ-titanium aluminide-based alloys are among the candidate materials for advanced engine applications because of their light weight, relatively good high-temperature mechanical properties and oxidation resistance. However, their application is currently limited by the relatively low levels of tensile ductility and fracture toughness exhibited by these materials at temperatures below approximately 600 °C. Various approaches such as: alloying to reduce tetragonality of the γ-TiAl unit cell and hence promote dislocation plasticity in this phase, for example [1], alloying to enhance twinning as a deformation mechanism [2], introduction of ductile grain-boundary precipitates to help accommodate plastic strain incompatibilities due to insufficient number of independent slip systems in γ-TiAl [3], etc., have been pursued with modest success. Another quite promising toughening and ductilizing mechanism for γ-TiAl based on the introduction of dispersed, metastable phases that can undergo a deformation-induced martensitic transformation has been utilized in the recent work of Grujicic and Dang [4].

The phenomenon of transformation enhanced toughness and ductility was first established by Zackay *et al.* back in 1967 [5]. Since then, record levels of ductility and fracture toughness have been reported in high-strength steels and ceramics undergoing martensitic transformation. For example, Haidemenopoulos [6] found a 25% increase in fracture toughness of VAR 4340 and AF 1410 steels due to a deformation-induced face-centred cubic–body-centred cubic (fcc → bcc) martensitic transformation in dispersed austenite without a significant loss in materials strength. Furthermore, manifold increase in fracture toughness, $K_{IC}$), has been reported in selected $ZrO_2$ based systems and ceramic matrices containing $ZrO_2$ second phase particles [7], in which a tetragonal–monoclinic stress-induced martensitic transformation takes place.

The ability of the Ti-base (bcc β-phase to undergo a martensitic transformation was utilized in the work of Grujicic and Dang [4] to induce dispersed-phase transformation toughening effects in γ-TiAl. It is well established, for example [8, 9] that martensitic transformation in the Ti-base β-phase can result in formation of one of the following two martensites: an α′ martensite with hexagonal close-packed (hcp) structure or an α″ martensite with a face-centred orthorhombic (fco) structure. Which of the two structures will form in a given alloy system is governed primarily by thermodynamic stability of the β-phase, which, in turn, is a function of the amount of the β-stabilizing elements (V, Nb, Mo, Fe, etc.) and temperature. The hcp α′ martensite is typically found in pure or low-alloyed Ti, while alloys containing β-stabilizing elements tend to form the fco α″ martensite. In addition, stress- and/or strain-induced martensite typically has the fco crystal structure. For example, Grujicic and Narayan [8, 9] observed a β → α″ stress-induced martensitic transformation in the Ti–Al–V–Fe β-phase.

From the transformation toughening point of view, the $\beta \rightarrow \alpha''$ martensitic transformation is preferred because it is accompanied by a positive volume change, and hence more effectively shields the crack tip and reduces the effective crack-tip stress intensity factor. In addition to the magnitude of the transformation volume change, the thermodynamic stability of the β-phase relative to the $\alpha''$ martensite is another factor affecting the extent of transformation toughening. To maximize the transformation toughening effects, the transformation volume change should be maximized, while thermodynamic stability should be maintained at an optimum level to ensure that the dispersed β-phase remains metastable with respect to martensite upon cooling to the ambient temperature but can undergo a deformation-induced martensitic transformation under the influence of the crack-tip stress and strain fields. In addition to the relative thermodynamic stability of the β-phase relative to martensite, high-temperature chemical compatibility between the β-phase particles and the γ-TiAl is required to ensure good thermal stability of the β–γ two-phase material. By carrying out a detailed thermodynamic analysis and experimental investigation of the effect of alloy composition on the thermodynamic stability of the β-phase and the magnitude of the transformation volume change, Grujicic and Narayan [8, 9] identified Ti–30/40Al–45/55 V (wt %) as the optimal chemical composition range of the β-phase in the Ti–Al–V–Fe system. Grujicic and Dang [4] subsequently carried out an experimental investigation of a two-phase γ-TiAl alloy containing 10 vol % of the Ti–40 Al–32 V–2 Fe (wt %) β-phase and found a two-fold increase in fracture toughness relative to that in the single-phase γ-TiAl processed under identical conditions. By carrying out a detailed microstructural examination of the fracture surfaces in the β–γ alloy, Grujicic and Dang [4] showed that the main toughening mechanism involves bridging of the cracks propagating along the γ-phase lamellar boundaries by the β-phase particles undergoing a stress-induced $\beta \rightarrow \alpha''$ martensite transformation accompanied by particle–matrix decohesion. While the crack bridging by ductile particles and fibres is studied extensively, for example [10], we are not aware of any work dealing with the interaction between martensitic transformation in the dispersed particles and their role in the crack bridging process. In the present two-part work, a numerical finite element analysis of γ-TiAl crack-bridging by transforming β-phase particles accompanied by particle–matrix decohesion is presented. Part I of this two-part paper deals with the derivation of β–γ interface and γ–γ lamellar boundary decohesion potentials through the use of molecular statics atomistic simulation method. These potentials are next used to derive the constitutive relations for the interfacial (continuum) elements that can be incorporated into a finite element analysis of a particle–matrix decohesion process. Such a finite element analysis is carried out in Part II of this two-part paper [11] to analyse the interaction between crack bridging by particles of the β-phase and particle–matrix decohesion.

The organization of Part I of this two-part paper is as follows: The embedded atom method (EAM) interatomic potentials used are presented in Section 2.1. The procedure used for construction of the computational crystal and the computational procedure for determination of the interface decohesion potentials are described in Sections 2.2 and 2.3, respectively. In Section 3, the results are presented and discussed. The main conclusions resulting from the present work are listed in Section 4. Derivation of the constitutive relations for the β–γ interfacial and γ–γ lamellar boundary elements is discussed in the appendix.

## 2. Computational procedure

### 2.1. Interatomic potentials

The interatomic potentials that account for the atomic interactions in the crystal are the required input for the atomistic simulations and therefore their reliability and accuracy are very critical for the atomistic simulations to be able to represent the materials behaviour faithfully. In contrast to the traditional pair potentials, the EAM interatomic potentials take into account, in an implicit way, the many-body effects and have therefore been proven more reliable in representing the atomic interactions in metals [12, 13]. Within the EAM scheme the total potential energy of the system is given as the sum of two terms: (a) the interaction of each atom with the local electron density associated with the remaining atoms in the system, called the embedding energy and; (b) a pair-like interaction reflecting the electrostatic interactions between the atomic cores. Thus, the total potential energy of a system containing $n$ atoms, $E_{tot}$, can be written as

$$E_{tot} = \sum_{i}^{n} F_i(\rho_i) + \frac{1}{2}\sum_{i}^{n}\sum_{j \neq i}^{n} \phi_{ij}(r_{ij}) \qquad (1)$$

where $F_i$ is the embedding energy of atom, i, i.e. the energy required to embed atom i into the electron density at location of atom i, $\rho_i$; and $\phi_{ij}(r_{ij})$ is the pairwise interaction between atoms i and j separated by the distance $r_{ij}$. The electron density at each site is computed from the superposition of spherically averaged atomic electron densities

$$\rho_i = \sum_{j \neq i}^{n} f_j^{\alpha}(r_{ij}) \qquad (2)$$

Here, $f_j^{\alpha}(r_{ij})$ is the atomic electron density at a distance $r_{ij}$ from the nucleus of atom j and the superscript α is used to specify the species of atom j.

In the present work, the EAM-type interatomic potentials are used for both the γ-TiAl phase and the β-Ti–V phase. γ-TiAl has an $L1_0$ type ordered structure, and therefore when carrying out atomistic simulations in this phase, one must account for the Ti–Ti, Al–Al and Ti–Al interactions and for the fact that the two atomic species reside on the separate sublattices. Farkas *et al.* [14] recently developed the necessary EAM-type potentials for γ-TiAl and showed that a reasonable agreement can be obtained between the model predictions and the experimentally measured properties of this phase. In the present work Farkas

potentials were used to describe Ti–Ti, Al–Al and Ti–Al interactions within the γ-TiAl phase.

The β-Ti–V phase has a disordered bcc structure, and to simplify the calculations the β-Ti–V phase was treated as a pseudomonoatomic phase composed of "effective" Ti–V atoms rather than individual Ti and V atoms. The derivation of the EAM potential functions for the pseudomonoatomic β-phase by applying an averaging scheme to the corresponding EAM functions of the constituent elements (Ti and V) was discussed in detail in our previous work [15]. The use of the pseudomonoatomic approximation for the Ti–V system appears appropriate because the two elements in question differ slightly in both the atomic mass (47.90 for Ti and 50.94 for V) and in the electronegativity (1.4 for Ti and 1.9 for V) [16]. In our previous atomistic simulation work [15], it was shown that the use of effective Ti–V potentials leads to reasonable prediction of a number of properties of the β-phase. In particular, the bcc structure was found to be unstable in pure Ti, metastable in Ti–15 at % V and stable in Ti–25 at % V relative to the hcp structure at 0 and 100 K, which is consistent with available thermodynamic data [17].

Atomistic simulations carried out in the present work were based on the use of γ-TiAl–β-Ti–V and γ–γ computational bicrystals containing three types of atoms, i.e. Ti and Al atoms associated with the γ-TiAl phase and effective Ti–V atoms constituting the Ti–V β-phase. Therefore, there are six distinct atomic pairs whose interactions (the $\phi_{ij}$ terms in Equation 1) must be known. As mentioned earlier the pair potentials for the Ti–Ti, Al–Al and Ti–Al pairs along with the corresponding embedding energy functions for the γ-phase have been determined by Farkas [14]. The effective Ti–V atom–effective Ti–V atom pair potential as well as the corresponding embedding energy have been derived in our previous work [15]. Hence there remain only two unknown interatomic parameters, the Ti–effective Ti–V atom and the Al–effective Ti–V atom pair potentials, which must be determined in order to be able to describe the atomic interactions completely in the β–γ computational bicrystals. The missing pair potentials $\phi_{i\beta}$ (i = Ti, Al, β = the effective Ti–V atom) are constructed in the present work using Johnson's approach [18]

$$\phi_{i\beta} = \frac{1}{2}\left[\frac{f_\beta(r_{\beta\beta})}{f_i(r_{ii})}\,\phi_{ii}(r_{ii}) + \frac{f_i(r_{ii})}{f_\beta(r_{\beta\beta})}\,\phi_{\beta\beta}(r_{\beta\beta})\right] \quad i = \text{Ti, Al} \tag{3}$$

where $f_\beta$ and $\phi_{\beta\beta}$ are, respectively, the atomic electron density and the pair potential functions of the β-Ti–V phase, which are obtained using the aforementioned pseudomonoatomic approximation [15].

## 2.2. Problem description

In the present analysis particles of the β-phase dispersed in the γ-matrix are assumed to be spherical in shape, of the same size and behave identically. Under such an assumption, the β–γ two-phase material can be partitioned into a regular three-dimensional array of hexagonal cylinders of the γ matrix each containing one β-phase particle, Fig. 1. A further simplification is next introduced that allows the particle crack-bridging process to be analysed as an axisymmetric problem. As shown by Tvergaard [19], the configuration shown in Fig. 1 can be reasonably well approximated by an infinite series of stacked circular cylinders each containing a spherical particle. One of such cylinders is shown in Fig. 2. To comply with the experimental observations of Grujicic and Dang [4] that the β-phase particles are precipitated along the γ matrix lamellar boundary, a $[1\,1\,1]_\gamma$ lamellar boundary that bisects the cylinder and the particle is introduced in Fig. 2. Furthermore, the orientation relations between the two phases are defined as: $[1\,1\,0]_\beta/[1\,1\,1]_\gamma$, $[0\,0\,1]_\beta/[0\,1\,1]_\gamma$ and $[1\,1\,0]_\beta/[2\,1\,1]_\gamma$. Also shown in Fig. 2, is the schematic of three β–γ (A, B, C) bicrystals

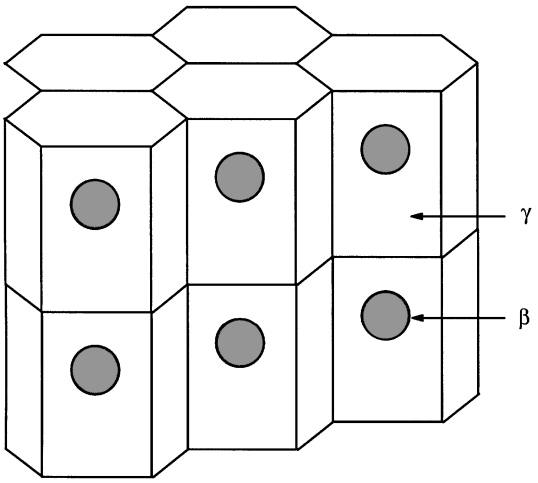


*Figure 1* Schematic representation of the uniform three-dimensional array of hexagonal cylinders of γ-TiAl matrix each containing a spherical β-phase particle.

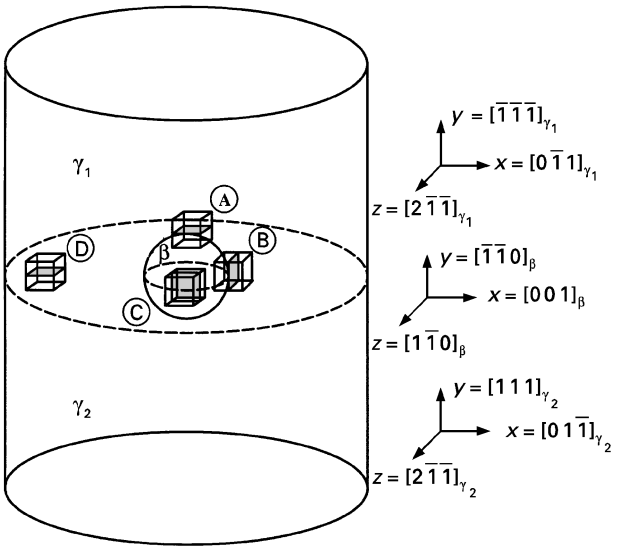


*Figure 2* Schematic representation of the circular cylinder showing a spherical β-phase particle located at the γ–γ lamellar interface. Schematics of the three β–γ bicrystals A, B and C and a γ–γ bicrystal D used in the calculation of the corresponding interfacial decohesion potentials are also shown.

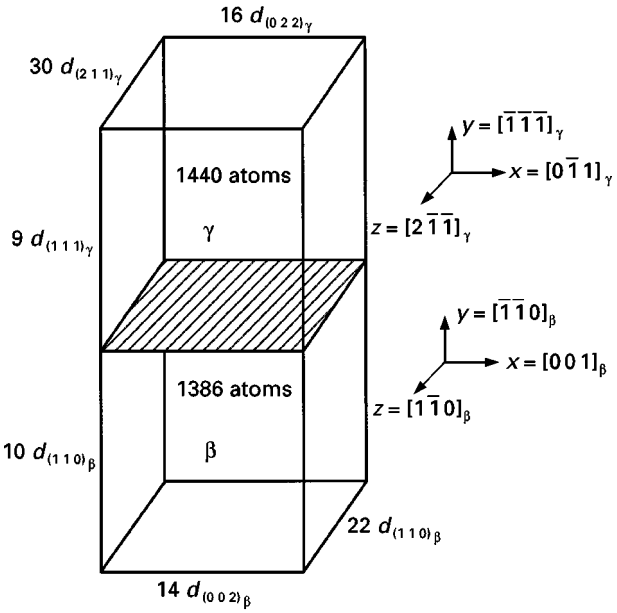


*Figure 3* Schematic representation of the β–γ bicrystal, designated as A in Fig. 2, used for determination of the $(1\,1\,0)_\beta/(1\,1\,1)_\gamma$ interfacial decohesion potential.

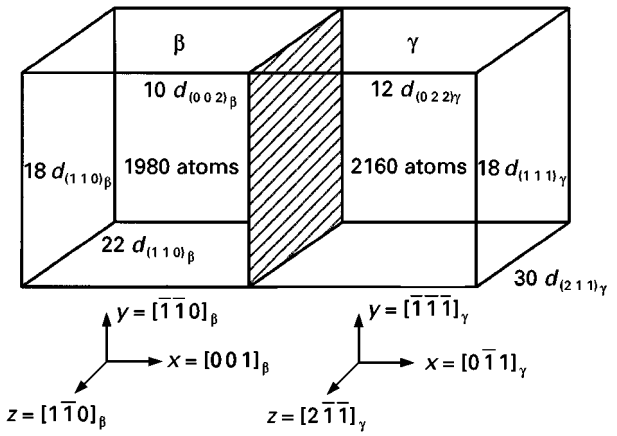


*Figure 4* Schematic representation of the β–γ bicrystal, designated as B in Fig. 2, used for determination of the $(0\,0\,1)_\beta/(0\,1\,1)_\gamma$ interfacial decohesion potential.

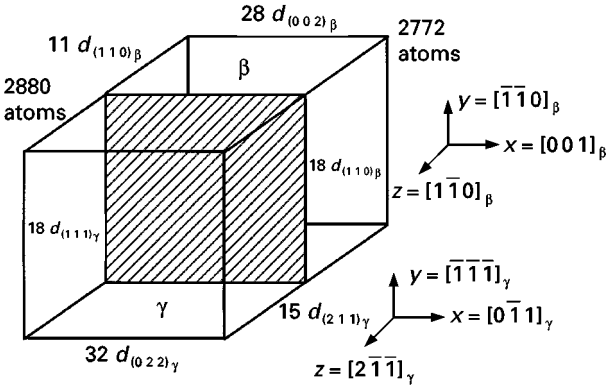


*Figure 5* Schematic representation of the β–γ bicrystal, designated as C in Fig. 2, used for determination of the $(1\,1\,0)_\beta/(2\,1\,1)_\gamma$ interfacial decohesion potential.

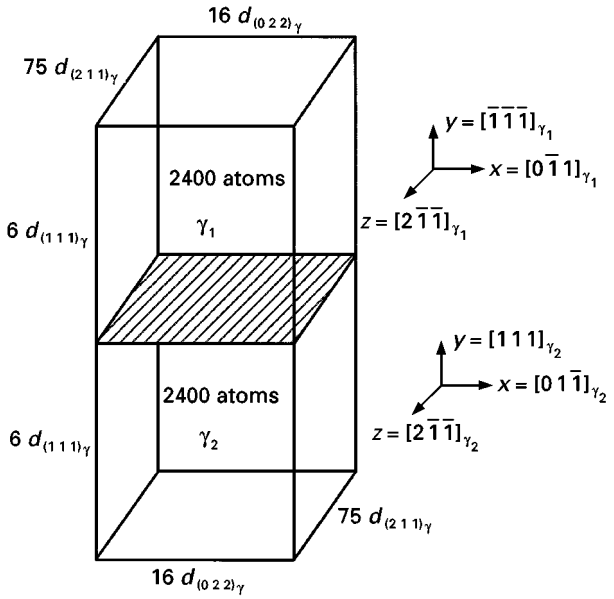


*Figure 6* Schematic representation of the γ–γ ($\gamma_1$–$\gamma_2$) bicrystal, designated as D in Fig. 2, used for determination of the $(1\,1\,1)_{\gamma 1}/(1\,1\,1)_{\gamma 2}$ interfacial decohesion potential.

and one γ–γ (D) bicrystal used in the atomistic simulation analysis of the β–γ and γ–γ interface structure and decohesion potentials. More detailed schematics of the four bicrystals, containing the information about the number of atoms, the orientation relationship and the sizes of the joined single crystals and the interface orientation, are shown in Figs 3–6. The single crystal sizes are expressed in terms of the number of interplanar spacings, $d_{(u\,v\,w)}$ of the $(u\,v\,w)$ planes.

The four atomistic bicrystals mentioned above are formed by bringing into contact a rectangular γ-TiAl single crystal with either a rectangular Ti–V β-phase single crystal or with a rectangular γ-TiAl single crystal. Prior to forming the bicrystals, the equilibrium lattice parameters at 0 K in each phase are determined by carrying out the potential energy minimization in each single crystal through the use of the conjugate gradient method [20]. For the $L1_0$ TiAl γ-phase the following lattice parameters are obtained: $a_\gamma = 0.3944$ nm and $c_\gamma = 0.4010$ nm, resulting in a $c_\gamma/a_\gamma$ ratio of 1.05, which is in fair agreement with its experimental counterpart $c_\gamma/a_\gamma = 1.03$ [21].

The β-phase with 15 at % V is chosen in the present work because it was found previously [22, 23] that at this level of vanadium, the bcc structure is metastable and undergoes martensitic transformation only in the presence of stress. When the amount of vanadium is below 10 at %, the bcc phase is unstable and transforms completely to martensite even in the absence of stress [22, 23]. Contrary, when the amount of vanadium is 20 at % or higher, the bcc phase remains stable even in the presence of a Mode I crack loaded to the stress level corresponding to the Griffith stress intensity factor [22, 23]. For the Ti–15 at % V bcc phase, the energy minimization procedure yielded the lattice parameter $a_\beta = 0.3186$ nm, which is in reasonable agreement with its experimental counterpart (0.322 nm) [8].

In addition to specifying the orientation of the two joined single crystals, the relative stacking of the atoms in the two structures must be defined. For example, in the case of bicrystal A, the $(1\,1\,1)_\gamma$ and $(1\,1\,0)_\beta$ planes, which are parallel to the β–γ interface, have, respectively, the ABCABC – and ABAB-type atomic stacking. The two single crystals are joined in such a way that the $(1\,1\,0)_\beta$ plane nearest to the interface "coincides" with the $(1\,1\,1)_\gamma$ plane that is next nearest to the interface and vice versa, yielding the stacking sequence $A_\gamma B_\gamma C_\gamma A_\gamma B_\gamma | A_\beta B_\beta A_\beta B_\beta \ldots$ .

## 2.3. Computation of interface structure

The equilibrium interface structure at 0 K is determined by minimizing the potential energy of each of the four bicrystals using the conjugate gradient method under flexible periodic boundary conditions in the two directions parallel to the interface and free surface boundary conditions in the direction normal to the interface. The use of free surface boundary conditions allows the spacing of the planes parallel to and near the interface to adjust to the differences in the atomic environment.

## 2.4. Computation of interface decohesion potential

The interface decohesion potential for each of the four bicrystals is determined by first regidly displacing the two single crystals in each case in the normal, n, and tangential, t and b, direction by different amounts. These three displacements are, respectively, designated as $U_n$, $U_t$ and $U_b$. The potential energy of the bicrystals is next minimized under the constraint that the average displacements of the atoms in the interface planes in each of the two joined crystals remain equal to the rigid displacements $U_n$, $U_t$ and $U_b$. The difference between the energies of the bicrystal in the displaced configuration and in the equilibrium configuration (obtained in Section 2.3.) expressed per unit area of the interface is then defined as the value of the interface decohesion potential, Φ, at given values of $U_n$, $U_t$ and $U_b$.

## 3. Results and discussion

The results of the molecular statics simulations of the equilibrium configuration of the three β–γ interfaces and the γ–γ lamellar boundary are shown in Figs 7–10. In each case, the projections of the atoms of the two phases on the interface–lamellar boundary plane are given as well as the projections on at least one of the planes normal to the interface plane. Also in each case, the interface dislocation arrays are marked as $D_1$ and $D_2$. A complete summary of the parameters characterizing the interfacial dislocation structure for

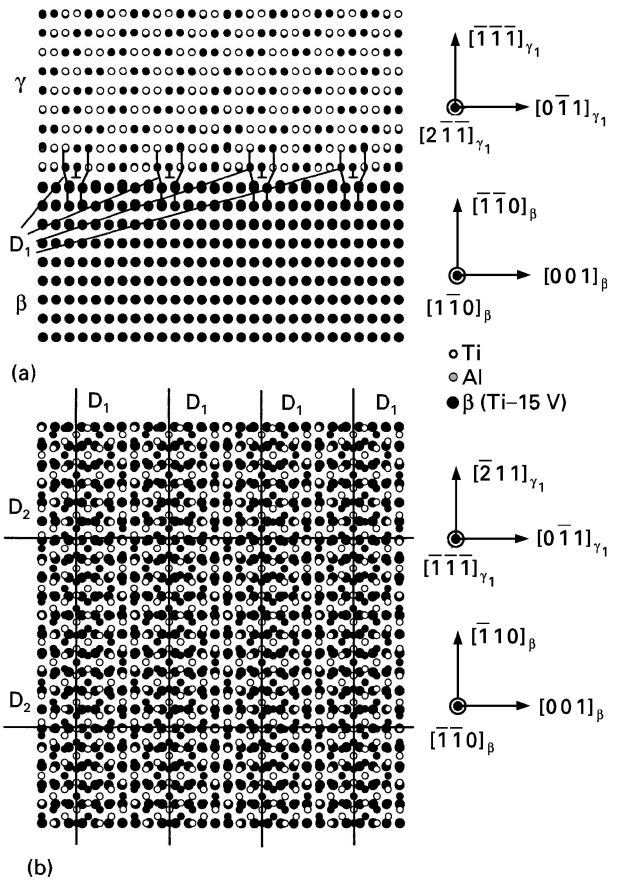


*Figure 7* Equillibrium configuration of the $(\bar{1}\,\bar{1}\,0)_\beta/(\bar{1}\,\bar{1}\,\bar{1})_\gamma$ interface (bicrystal A). Atomic positions projected onto (a) the $(1\,\bar{1}\,0)_\beta/(2\,\bar{1}\,\bar{1})_\gamma$ plane, and (b) the $(\bar{1}\,\bar{1}\,0)_\beta/(\bar{1}\,\bar{1}\,\bar{1})_\gamma$ interface plane (interfacial dislocations are marked as $D_1$ and $D_2$).

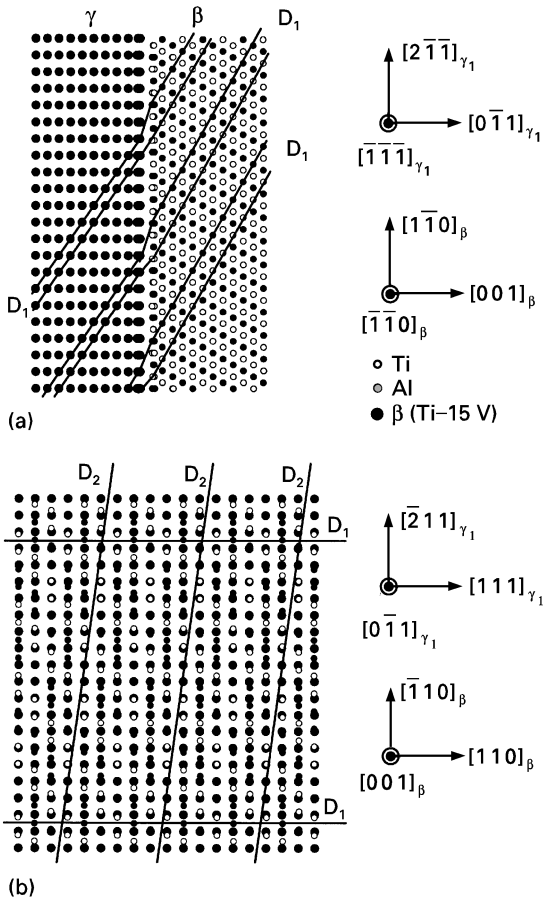


*Figure 8* Equilibrium configuration of the $(0\,0\,1)_\beta/(0\,\bar{1}\,1)_\gamma$ interface (bicrystal B). Atomic positions projected onto (a) the $(\bar{1}\,\bar{1}\,0)_\beta/(\bar{1}\,\bar{1}\,\bar{1})_\gamma$ plane, and (b) the $(0\,0\,1)_\beta/(0\,\bar{1}\,1)_\gamma$ interface plane (interfacial dislocations are marked as $D_1$ and $D_2$).

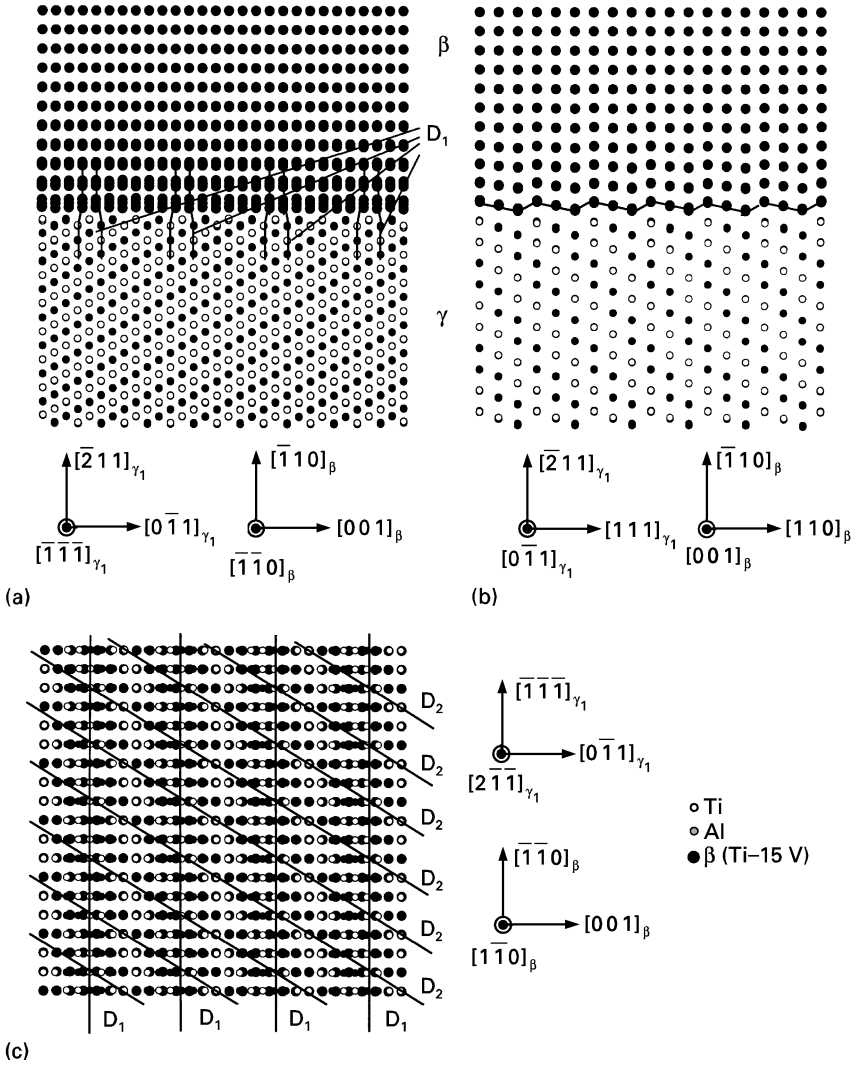


*Figure 9* Equilibrium configuration of the $(1\bar{1}0)_\beta/(2\bar{1}\bar{1})_\gamma$ interface (bicrystal C). Atomic positions projected onto (a) the $(\bar{1}\bar{1}0)_\beta/(\bar{1}\bar{1}\bar{1})_\gamma$ plane, (b) the $(\bar{0}\bar{0}\bar{1})_\beta/(0\bar{1}1)_\gamma$ plane, and (c) the $(1\bar{1}0)_\beta/(2\bar{1}\bar{1})_\gamma$ interface plane (interfacial dislocations are marked as $D_1$ and $D_2$).

each of the four cases including the line direction, the Burger's vector and the dislocation spacing is given in Table I.

The results of the calculation of the decohesion potential, $\Phi$, for the four bicrystals are shown in Figs 11–14. In each case, the variation of $\Phi$ with the normal displacement, $U_n$, at various values of the tangential displacement, $U_t$, and $U_b = 0$ is given in the respective figure (a) and the variation of $\Phi$ with the tangential displacement, $U_t$, at various values of the tangential displacement, $U_b$, and the zero value of normal displacement, $U_n$, is shown in the respective figure (b). The general behaviour of the interfacial potential with the variation in the three displacements can be summarized as follows:

1. For the pure normal decohesion process where $U_t = U_b = 0$, the interface potential increases monotonically with the normal displacement, $U_n$, and asymptotically approaches a value defined as the work of decohesion, $\Phi_{dec}$.

2. At non-zero values of the tangential displacements, for example, for $U_t \neq 0$ and $U_b = 0$ as in Fig. 11a, the decohesion potential first decreases and then increases with the normal displacement, $U_n$.

3. The shear behaviour of the interface is periodic with the periodic lengths, which can be related to the spacing of the interfacial dislocations. For example, the periodic length for $\Phi$ in Fig. 11b is equal to the spacing, $\lambda$, of the interfacial dislocations, $D_1$, in Fig. 7.

4. The pure shear behaviour is unstable in some cases because perturbations in the normal, $U_n$ (e.g. Fig. 11a) or in the orthogonal shear displacements (e.g. Fig. 11b) give rise to a reduction in energy.

5. In some cases as in Fig. 13b, the shear behaviour is not symmetric. This appears to be the result of the non-planar step and ledge character of the interface, Fig. 9b.

Because the interfacial decohesion potentials for the interfaces in the β–γ bicrystals (A, B and C) will be used in Part II of this two-part paper [11] for an axisymmetric finite element analysis of the crack-bridging process by β-phase particles in the presence of particle–matrix decohesion, it is useful to have the three β–γ decohesion potentials derived in the present

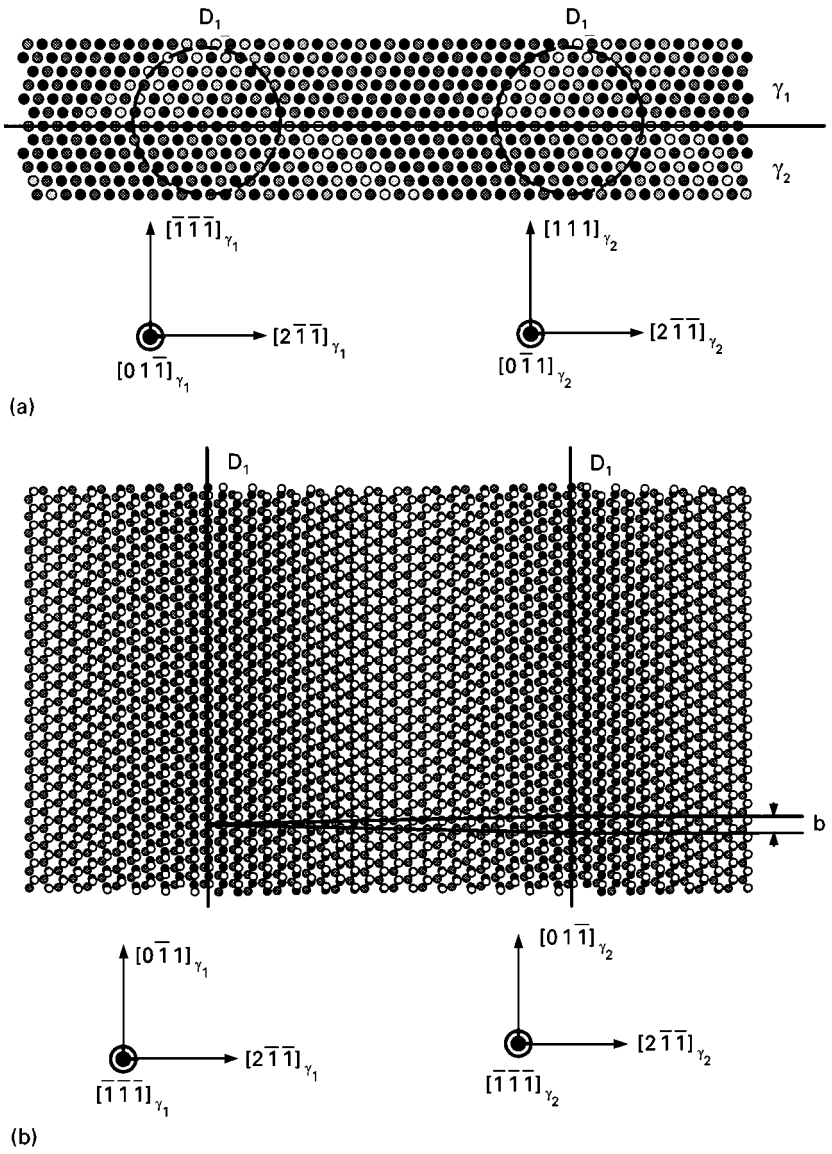


*Figure 10* Equilibrium configuration of the $(\bar{1}\,\bar{1}\,\bar{1})_{\gamma 1}/(1\,1\,1)_{\gamma 2}$ interface (bicrystal D). Atomic positions projected onto (a) the $(0\,1\,\bar{1})_{\gamma 1}/(0\,\bar{1}\,1)_{\gamma 2}$ plane, and (b) the $(\bar{1}\,\bar{1}\,\bar{1})_{\gamma 1}/(1\,1\,1)_{\gamma 2}$ interface plane (interfacial screw dislocations are marked as $D_1$).

work expressed using the same functional form. The fact that pure shear is unstable in some cases, rules out the use of the interface potential function proposed by both Needleman [24] and Socrate [25]. Furthermore, due to the non-symmetric character of the interface shear, the universal function for ideal shear proposed by Bozzolo *et al.* [26] could also not be used. After testing a number of functions, the following function is found to mimic best the overall relationship between $\Phi$ and $U_n$, $U_t$ and $U_b$ for the three $\beta$–$\gamma$ interfaces

$$\Phi = \sigma_{max}\delta_n\left[e - \left(\frac{U_n}{\delta_n} + 1\right)\exp^{[(U_n/\delta_n)+1]}\right] + \frac{1}{2}\alpha_0\left(\frac{6U_n}{\delta_n} + 1\right)\exp^{(6U_n/\delta_n)} \left\{\alpha_1 + \left[\alpha_2 \sin\frac{4\pi(U_t - 2)}{\lambda_t} + \cos\left(\frac{2\pi U_t}{\lambda_t} + \alpha_3\right) + \alpha_4\right]\left(\alpha_5 + \cos\frac{2\pi U_b}{\lambda_b}\right)\right\} \quad (4)$$

Furthermore, the $\gamma$–$\gamma$ lamellar boundary decohesion potential is found to comply with Equation 4. Table II gives a summary of the parameters appearing in Equation 4 for the four interfaces–boundaries considered here.

It should be noted that several parameters appearing in Equation 4 have a particular physical meaning:

1. $\sigma_{max}$ is the normal interface strength associated with the pure normal decohesion processes, $U_b = U_t = 0$, and is associated with the normal interfacial displacement, $U_n = \delta_n$.
2. $\lambda_b$ and $\lambda_t$ are the periodic lengths for pure shear in the two shear directions b and t, respectively, and are related to the spacing of the corresponding interfacial dislocations.
3. The shear interface strengths in the two directions, $\tau_{max,b}$ and $\tau_{max,t}$, are very complex functions of the parameters and occur at $U_b \cong 0.25\lambda_b$, $U_n = U_b = 0$ and $U_t = 0.25\lambda_t$, $U_n = U_b = 0$, respectively.

TABLE I Parameters characterizing interfacial dislocation for the three β–γ and one γ–γ interfaces analysed in the present work

| Parameter | Dislocation type | |
|---|---|---|
| | $D_1$ | $D_2$ |
| $(\bar{1}\,\bar{1}\,0)_\beta/(\bar{1}\,\bar{1}\,\bar{1})_\gamma$ interface: bicrystal A | | |
| Line direction, 1 | $[1\,\bar{1}\,0]_\beta$<br>$[2\,\bar{1}\,\bar{1}]_\gamma$ | $[0\,\bar{0}\,1]_\beta$<br>$[0\,\bar{1}\,1]_\gamma$ |
| Burger's vector, b | $1/2\ a_\beta\ [0\,0\,1]_\beta$<br>$1/2\ a_\gamma c_\gamma/(a_\gamma^2 + c_\gamma^2)^{1/2}[0\,\bar{1}\,1]_\gamma$ | $4\ a_\beta/(2)^{1/2}[\bar{1}\,1\,0]_\beta$<br>$4\ a_\gamma c_\gamma/(a_\gamma^2 + 5\ c_\gamma^2)^{1/2}[2\,1\,1]_\gamma$ |
| Dislocation spacing, λ | $7/2\ a_\beta$<br>$4\ a_\gamma c_\gamma/(a_\gamma^2 + c_\gamma^2)^{1/2}$ | $10\ a_\beta/(2)^{1/2}$<br>$14\ a_\gamma c_\gamma/(a_\gamma^2 + 5\ c_\gamma^2)^{1/2}$ |
| $(0\,0\,1)_\beta/(0\,\bar{1}\,1)_\gamma$ interface: bicrystal B | | |
| Line direction, 1 | $[\bar{1}\,\bar{1}\,0]_\beta$<br>$[\bar{1}\,\bar{1}\,\bar{1}]_\gamma$ | $[3\,\bar{4}\,0]_\beta$<br>$[\bar{3}\,2\,2]_\gamma$ |
| Burger's vector, b | $2\ a_\beta/(2)^{1/2}\ [\bar{1}\,1\,0]_\beta$<br>$2\ a_\gamma c_\gamma/(a_\gamma^2 + 5\ c_\gamma^2)^{1/2}[\bar{2}\,1\,1]_\gamma$ | $a_\beta/5[4\,3\,0]_\beta$<br>$a_\gamma c_\gamma/(9\ a_\gamma^2 + 25\ c_\gamma^2)^{1/2}[4\,3\,3]_\gamma$ |
| Dislocation spacing, λ | $7\ a_\beta/(2)^{1/2}$<br>$10\ a_\gamma c_\gamma/(a_\gamma^2 + 5\ c_\gamma^2)^{1/2}$ | $21\ a_\beta/5$<br>$20\ a_\gamma c_\gamma/(9\ a_\gamma^2 + 25\ c_\gamma^2)^{1/2}$ |
| $(1\,\bar{1}\,0)_\beta/(2\,\bar{1}\,\bar{1})_\gamma$ interface: bicrystal C | | |
| Line direction, 1 | $[1\,\bar{1}\,0]_\beta$<br>$[\bar{1}\,\bar{1}\,\bar{1}]_\gamma$ | $[3\,3\,7]_\beta$<br>$[\bar{1}\,\bar{1}\,\bar{3}]_\gamma$ |
| Burger's vector, b | $1/2\ a_\beta\ [0\,0\,1]_\beta$<br>$1/2\ a_\gamma c_\gamma/(a_\gamma^2 + c_\gamma^2)^{1/2}[0\,\bar{1}\,1]_\gamma$ | $a_\beta/(134)^{1/2}[\bar{7}\,\bar{7}\,6]_\beta$<br>$a_\gamma c_\gamma/(a_\gamma^2 + 65\ c_\gamma^2)^{1/2}[4\,7\,1]_\gamma$ |
| Dislocation spacing, λ | $7/2\ a_\beta$<br>$4\ a_\gamma c_\gamma/(a_\gamma^2 + c_\gamma^2)^{1/2}$ | $21\ a_\beta/(134)^{1/2}$<br>$22\ a_\gamma c_\gamma/(a_\gamma^2 + 65\ c_\gamma^2)^{1/2}$ |
| $(1\,\bar{1}\,0)_\beta/(2\,\bar{1}\,\bar{1})_\gamma$ interface: bicrystal D | | |
| Line direction, 1 | $[0\,\bar{1}\,1]_\gamma$ | |
| Burger's vector, b | $1/2\ a_\gamma c_\gamma/(a_\gamma^2 + c_\gamma^2)^{1/2}[0\,\bar{1}\,1]_\gamma$ | |
| Dislocation spacing, λ | $25/2\ a_\gamma[(a_\gamma^2 + 2\ c_\gamma^2)/(a_\gamma^2 + c_\gamma^2)]^{1/2}$ | |

The magnitude of the interface decohesion potential in the limit $U_n \to \infty$, relative to its equilibrium magnitude at $U_n = U_b = U_t = 0$, is generally termed the work of decohesion and is taken to be in the range of 1–10 J m$^{-2}$. The results given in Table II are generally consistent with this range with the work of decohesion for the γ–γ lamellar interface being one-third–one-half of the ones for the three β–γ interfaces. The normal interface strength, $\sigma_{max}$, is generally assumed to be 0.01–0.02 times the material Young's modulus, which in the present case yields 0.7–1.4 GPa for the β-phase and 1.6–3.2 GPa for the γ-phase. The normal interface strength data given in Table II are consistent with this range of values only for the γ-phase. For the β-phase, the $\sigma_{max}$ data given in Table II are larger by a factor five–ten. Our preliminary work has shown that the magnitude of $\sigma_{max}$ is sensitive to the magnitude of the atomic interaction cut-off radius and that $\sigma_{max}$ can be reduced by about one-half if the atomic interaction cut-off radius is increased to include the contribution of the third nearest neighbours.

As for the shear interface strength, it is generally assumed to be a relatively small fraction of $\sigma_{max}$. An examination of the results given in Table II, shows that this is true for the case of the $(1\,1\,0)_\beta/(1\,1\,1)_\gamma$ interface (bicrystal A) as well as for the $(1\,1\,1)_{\gamma1}/(1\,1\,1)_{\gamma2}$ lamellar boundary. In addition, the shear resistances in the b and t directions are quite similar in the case of the bicrystal A. The latter finding is consistent with the dislocation structure of the corresponding β–γ interface for which the magnitude of the Burger's vector and the dislocation spacings are comparable in the two shear directions. For the β–γ interfaces in bicrystals B and C, the shear resistances in the two directions are quite different from each other and, as in the case of $\tau_{max,t}$ for bicrystal C, the shear resistance can be significantly larger than $\sigma_{max}$. This finding is a direct consequence of the non-planar interface morphology in bicrystal C, which consists of steps and ledges aligned in the b direction. Similarly, the presence of a single array of dislocations in the case of γ–γ lamellar boundary (bicrystal D) causes the two shear resistances, $\tau_{max,t}$ and $\sigma_{max,b}$ to differ by more than an order of magnitude.

## 4. Conclusions

Based on the results obtained in the present work, the following conclusions can be drawn:

1. The decohesion potential for the β–γ interfaces and the γ–γ lamellar boundary are closely related to the equilibrium dislocation structure of the corresponding interface–boundary.

2. For the three β–γ interfaces studied in the present work, the normal interface strength is found to vary by only about 40%.

3. The shear strength, on the other hand, can vary by as much as a factor of 20 even for the same interface, depending on the direction of shear. These

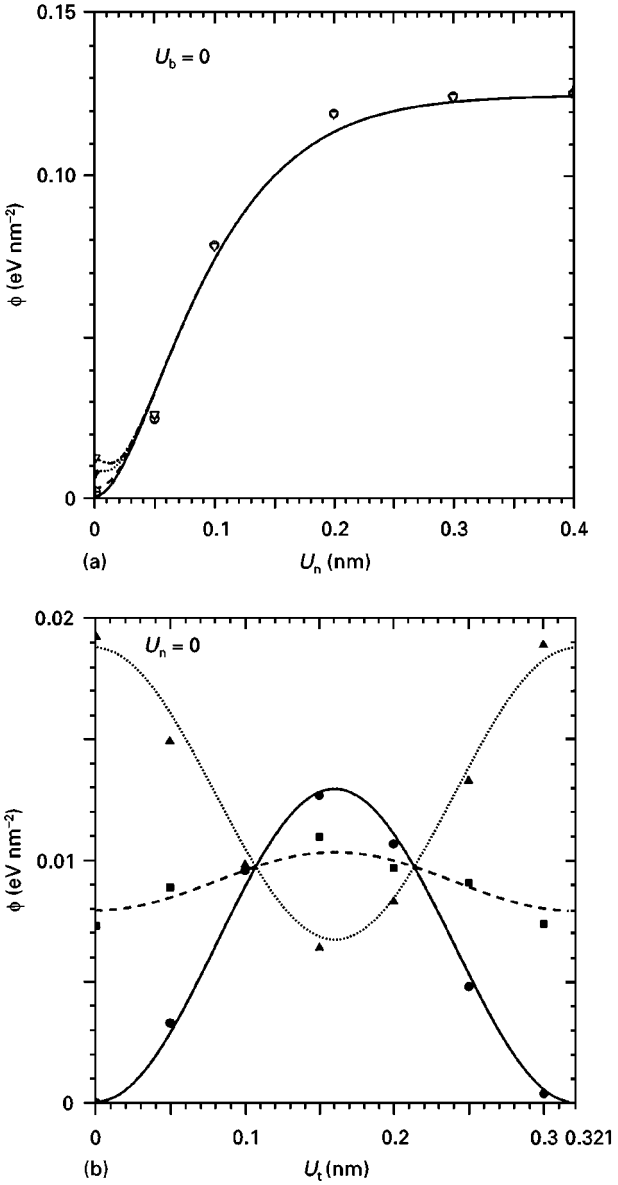


*Figure 11* Variation of the decohesion potential for the $(1\,1\,0)_\beta/(1\,1\,1)_\gamma$ interface with (a) normal displacement, $U_n$, in the $[\bar{1}\,\bar{1}\,0]_\beta/[\bar{1}\,\bar{1}\,\bar{1}]_\gamma$ direction and (b) tangential displacements, $U_t$ and $U_b$, in the $[0\,0\,1]_\beta/[0\,\bar{1}\,1]_\gamma$ and $[1\,\bar{1}\,0]_\beta/[2\,\bar{1}\,\bar{1}]_\gamma$ directions, respectively. For (a) $U_t$: (—) 0 nm, (— —) 0.05 nm, ( $\cdots$ ) 0.1 nm, (–·–) 0.15 nm. For (b) $U_b$: (—) 0 nm, (— —) 0.1 nm, ( $\cdots$ ) 0.2 nm.

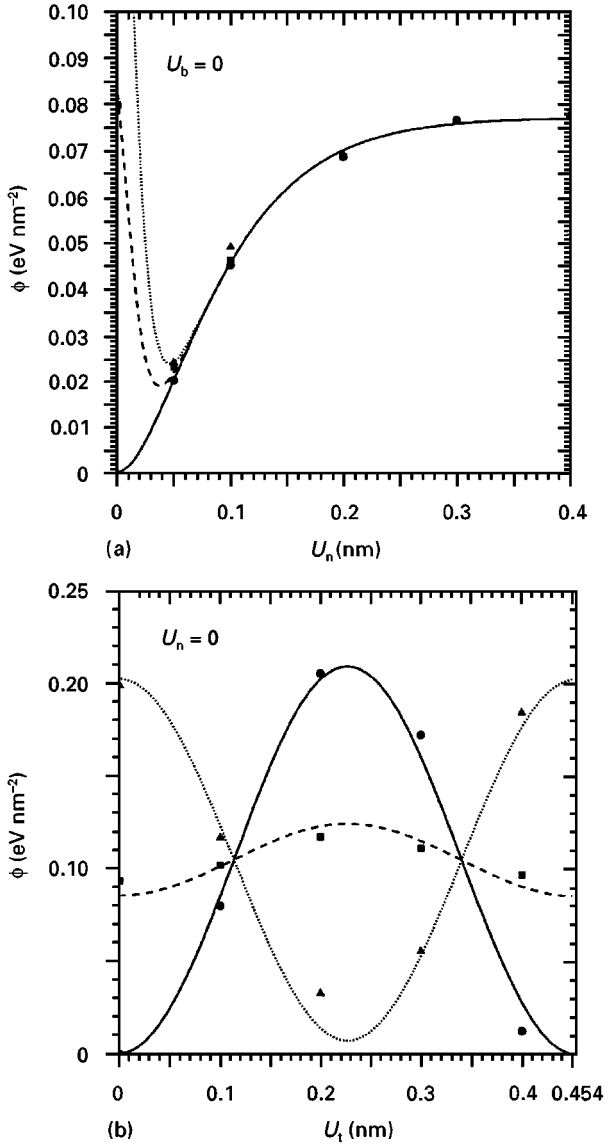


*Figure 12* Variation of the decohesion potential for the interface $(0\,0\,1)_\beta/(0\,1\,1)_\gamma$ with (a) normal displacement, $U_n$, in the $[0\,0\,1]_\beta/[0\,\bar{1}\,1]_\gamma$ direction and (b) tangential displacements, $U_t$ and $U_b$, in the $[\bar{1}\,\bar{1}\,0]_\beta/[\bar{1}\,\bar{1}\,\bar{1}]_\gamma$ and $[1\,\bar{1}\,0]_\beta/[2\,\bar{1}\,\bar{1}]_\gamma$ directions, respectively. For (a) $U_t$: (—) 0 nm, (— —) 0.1 nm, ( $\cdots$ ) 0.2 nm. For (b) $U_b$: (—) 0 nm, (— —) 0.1 nm, ( $\cdots$ ) 0.2 nm.

differences are a direct result of the type, the Burger's vector magnitude and the spacing of the dislocations dominating the structure of the given interface.

4. The interface potentials for all the interfaces studied in the present work can be described using the same functional form.

## Acknowledgements

The work presented here has been supported by the National Science Foundation under Grants DMR-9317804 and CMS-9531930 and the US Army Research Office, Grant DAAH04-96-1-0197. The authors are indebted to Drs Bruce A. MacDonald and William A. Spitzig of NSF and Dr Wilbur C. Simmons of ARO for the continuing interest in the present work. The help of Professor D. Farkas in providing us with the TiAl EAM potentials and the help of Professor D. Parks of Massachusetts Institute of Technology for sharing the unpublished results with us are greatly appreciated.

## Appendix

### A.1. Implementation of the interface decohesion potential in the finite element method

In Part II of the present work [11], the interface decohesion potentials developed in Section 2.4. are used in conjunction with the commercial finite element code ABAQUS [27] to analyse the crack-bridging process in the presence of particle–matrix decohesion. The interface decohesion potentials are incorporated into a user element library (UEL) subroutine that allows the user to define the contribution of the interfacial (continuum) elements to the global

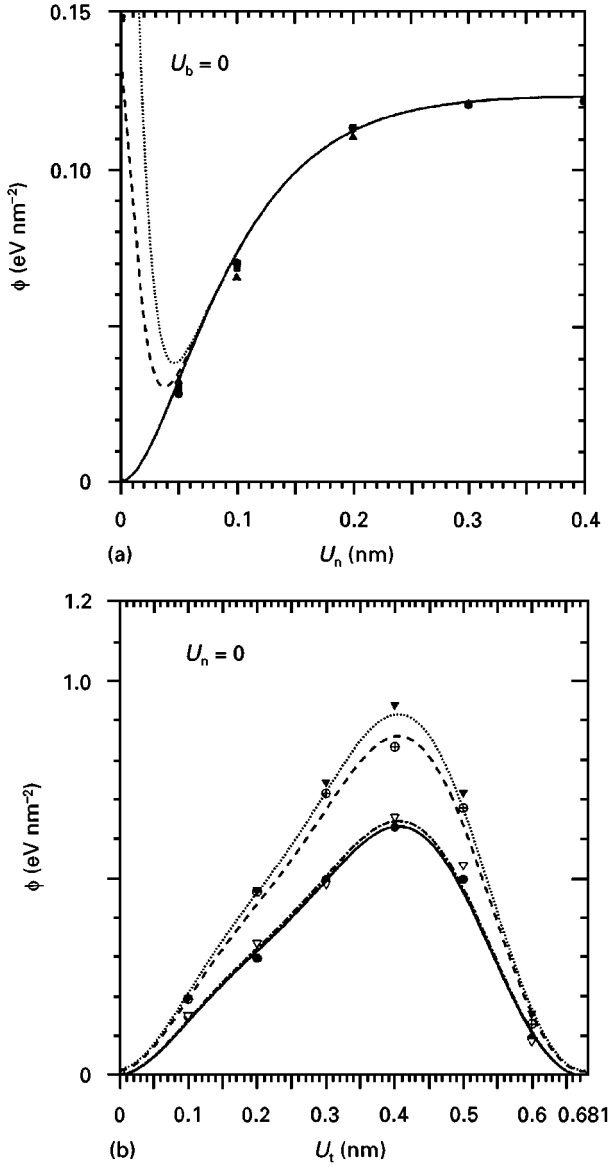


*Figure 13* Variation of the decohesion potential for the interface $(1\,1\,0)_\beta/(2\,1\,1)_\gamma$ with (a) normal displacement, $U_n$, in $[1\,\bar{1}\,0]_\beta/[2\,\bar{1}\,\bar{1}]_\gamma$ direction and (b) tangential displacements, $U_t$ and $U_b$, in the $[\bar{1}\,\bar{1}\,0]_\beta/[\bar{1}\,\bar{1}\,\bar{1}]_\gamma$ and $[0\,0\,1]_\beta/[0\,\bar{1}\,1]_\gamma$ directions, respectively. For (a) $U_t$: (—) 0 nm, (— —) 0.1 nm, ( $\cdots$ ) 0.2 nm. For (b) $U_b$: (—) 0 nm, (— —) 0.1 nm, ( $\cdots$ ) 0.2 nm, (–·–) 0.3 nm.

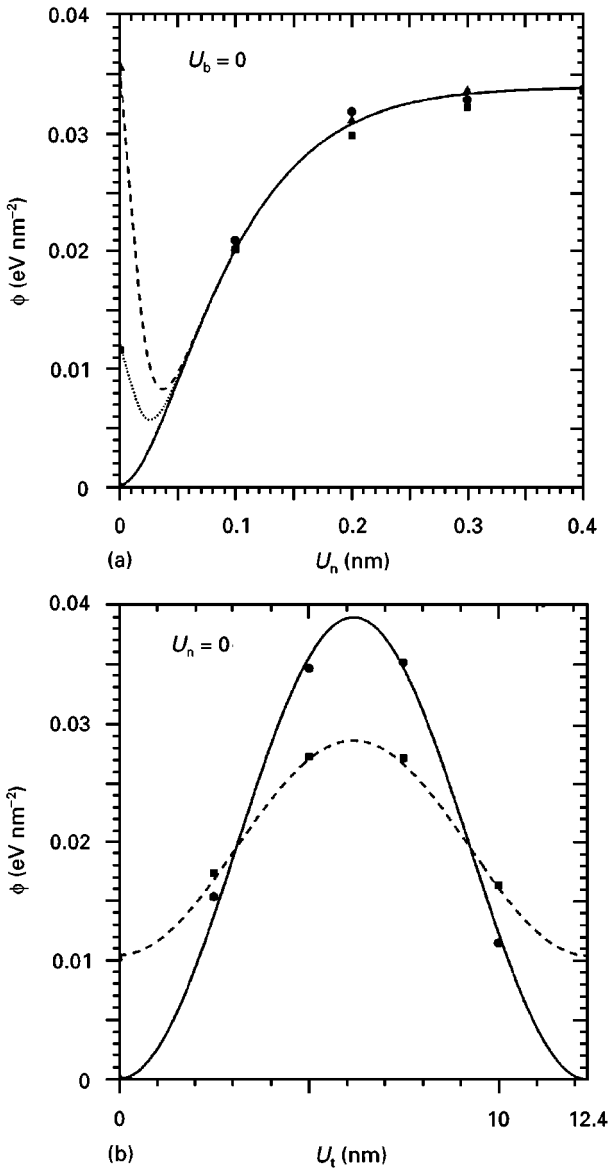


*Figure 14* Variation of the decohesion potential for the interface $(1\,1\,1)_{\gamma1}/(1\,1\,1)_{\gamma2}$ with (a) normal displacement, $U_n$, in the $[\bar{1}\,\bar{1}\,\bar{1}]_{\gamma1}/[1\,1\,1]_{\gamma2}$ direction and (b) tangential displacements, $U_t$ and $U_b$, in the $[0\,\bar{1}\,1]_{\gamma1}/[0\,1\,\bar{1}]_{\gamma2}$ and $[2\,\bar{1}\,\bar{1}]_{\gamma1}/[2\,\bar{1}\,\bar{1}]_{\gamma2}$ directions, respectively. For (a) $U_t$: (—) 0 nm, (— —) 5 nm, ( $\cdots$ ) 10 nm. For (b) $U_b$: (—) 0 nm, (— —) 0.1 nm.

TABLE II Decohesion potential parameters for the three β–γ and one γ–γ interfaces analysed in the present work

| Parameter | Interface type | | | |
|---|---|---|---|---|
| | $(1\,1\,0)_\beta/(1\,1\,1)_\gamma$ | $(0\,0\,1)_\beta/(0\,1\,1)_\gamma$ | $(1\,1\,0)_\beta/(2\,1\,1)_\gamma$ | $(1\,1\,1)_{\gamma1}/(1\,1\,1)_{\gamma2}$ |
| Designation | A | B | C | D |
| n-direction | $[\bar{1}\,\bar{1}\,0]_\beta/[\bar{1}\,\bar{1}\,\bar{1}]_\gamma$ | $[0\,0\,1]_\beta/[0\,\bar{1}\,1]_\gamma$ | $[1\,\bar{1}\,0]_\beta/[2\,\bar{1}\,\bar{1}]_\gamma$ | $[\bar{1}\,\bar{1}\,\bar{1}]_{\gamma1}/[1\,1\,1]_{\gamma2}$ |
| t-direction | $[0\,0\,1]_\beta/[0\,\bar{1}\,1]_\gamma$ | $[\bar{1}\,\bar{1}\,0]_\beta/[\bar{1}\,\bar{1}\,\bar{1})_\gamma$ | $[\bar{1}\,\bar{1}\,0]_\beta/[\bar{1}\,\bar{1}\,\bar{1}]_\gamma$ | $[0\,\bar{1}\,1]_{\gamma1}/[0\,1\,\bar{1}]_{\gamma2}$ |
| b-direction | $[1\,\bar{1}\,0]_\beta/[2\,\bar{1}\,\bar{1}]_\gamma$ | $[1\,\bar{1}0]_\beta/[2\,\bar{1}\,\bar{1})_\gamma$ | $[0\,0\,1]_\beta/[0\,\bar{1}\,1]_\gamma$ | $[2\,\bar{1}\,\bar{1}]_{\gamma1}/[2\,\bar{1}\,\bar{1}]_{\gamma2}$ |
| $\delta_n$, nm | 0.05 | 0.05 | 0.05 | 0.05 |
| $\lambda_t$, nm | 0.321 | 0.454 | 0.681 | 12.35 |
| $\lambda_b$, nm | 0.454 | 0.454 | 0.321 | 0.578 |
| $\alpha_0$ | − 0.013 | − 0.21 | − 0.148 | − 0.039 |
| $\alpha_1$ | − 1.5 | − 1 | 0.42 | − 1 |
| $\alpha_2$ | 0 | 0 | − 0.2 | 0 |
| $\alpha_3$ | 0 | 0 | − 3.42 | 0 |
| $\alpha_4$ | 0.5 | 0 | 1.17 | 0 |
| $\alpha_5$ | 0 | 0 | − 5 | 0 |
| $\sigma_{max}$, GPa | 7.37 | 4.57 | 7.29 | 2.01 |
| $\tau_{max,t}$, GPa | 1.09 | 11.77 | 29.2 | 0.160 |
| $\tau_{max,b}$, GPa | 1.11 | 5.60 | 1.20 | 1.65 |
| $\Phi$ ($U_n \to \infty$), J m$^{-2}$ | 2.02 | 1.25 | 2.03 | 0.561 |

finite element model. In other words, for the given nodal displacements of the interface elements provided to UEL by ABAQUS, the contribution of the elements to the global vector of residual forces and to the global Jacobian (element stiffness matrix) is determined in the UEL subroutine and passed to ABAQUS. The implementation of the interface decohesion potential in the UEL subroutine is discussed below.

Before implementing in the UEL subroutine, the decohesion potentials developed in the present work are simplified by averaging their shear behaviour in each case. This is done in order to comply with the axisymmetric geometry of a circular cylinder, Fig. 2. We are currently working on crystal plasticity based modelling of the crack-bridging process [28] in which no simplifications are introduced into the decohesion potential functions developed in the present work.

Each interface element is defined as a four-node isoparametric element on the β–γ interface or γ–γ lamellar boundary S, as shown schematically in Fig. A1. In the undeformed configuration (not shown for brevity), nodes 1 and 4, and nodes 2 and 3 coincide, respectively. A local co-ordinate system, consistent with the directions that are tangent, t, and normal, n, to the interface, is next assigned to the each element. This is done by introducing two "internal nodes", A and B, located at the midpoints of the lines 1–2 and 3–4, connecting the corresponding interface nodes of the β-phase particle and γ-TiAl matrix.

The interface displacements at the internal nodes A and B are expressed in terms of the displacements of the element nodes 1–4 as in the global co-ordinate system $z$–$r$

$$U_{\mathrm{n}}^{\mathrm{A}} = (U_z^4 - U_z^1)\cos\theta - (U_r^4 - U_r^1)\sin\theta \qquad \text{(A1)}$$

$$U_{\mathrm{t}}^{\mathrm{A}} = (U_z^4 - U_z^1)\sin\theta - (U_r^4 - U_r^1)\cos\theta \qquad \text{(A2)}$$

$$U_{\mathrm{n}}^{\mathrm{B}} = (U_z^3 - U_z^2)\cos\theta - (U_r^3 - U_r^2)\sin\theta \qquad \text{(A3)}$$

$$U_{\mathrm{t}}^{\mathrm{B}} = (U_z^3 - U_z^2)\sin\theta - (U_r^3 - U_r^2)\cos\theta \qquad \text{(A4)}$$

An isoparametric co-ordinate η is next introduced along the tangent direction with $\eta(\mathrm{A}) = -1$ and $\eta(\mathrm{B}) = 1$ and two linear Lagrangian interpolation functions are defined as $N_{\mathrm{A}}(\eta) = (1-\eta)/2$ and $N_{\mathrm{B}}(\eta) = (1+\eta)/2$.

The interpolation functions given above allow the normal and the tangential components of the interface displacements to be expressed in the form of their values at the internal nodes A and B

$$U_{\mathrm{t}}(\eta) = N_{\mathrm{A}}(\eta)U_{\mathrm{t}}^{\mathrm{A}} + N_{\mathrm{B}}(\eta)U_{\mathrm{t}}^{\mathrm{B}} \qquad \text{(A5)}$$

$$U_{\mathrm{n}}(\eta) = N_{\mathrm{A}}(\eta)U_{\mathrm{n}}^{\mathrm{A}} + N_{\mathrm{B}}(\eta)U_{\mathrm{n}}^{\mathrm{B}} \qquad \text{(A6)}$$

The tangential and normal components of the forces at modes A and B, i.e. $F_{\mathrm{t}}^{\mathrm{A}}$, $F_{\mathrm{t}}^{\mathrm{B}}$, $F_{\mathrm{n}}^{\mathrm{A}}$, $F_{\mathrm{n}}^{\mathrm{B}}$, which are work conjugates of the corresponding nodal displacements $U_{\mathrm{t}}^{\mathrm{A}}$, $U_{\mathrm{t}}^{\mathrm{B}}$, $U_{\mathrm{n}}^{\mathrm{A}}$ and $U_{\mathrm{n}}^{\mathrm{B}}$ are next determined through the application of the virtual work to the interfacial element

$$\int_{-1}^{1} \delta\Phi(\eta) L\pi r(\eta)\, d\eta = \sum_{I=n,\mathrm{t}} \sum_{N=\mathrm{A,B}} F_I^N \delta U_I^N \qquad \text{(A7)}$$

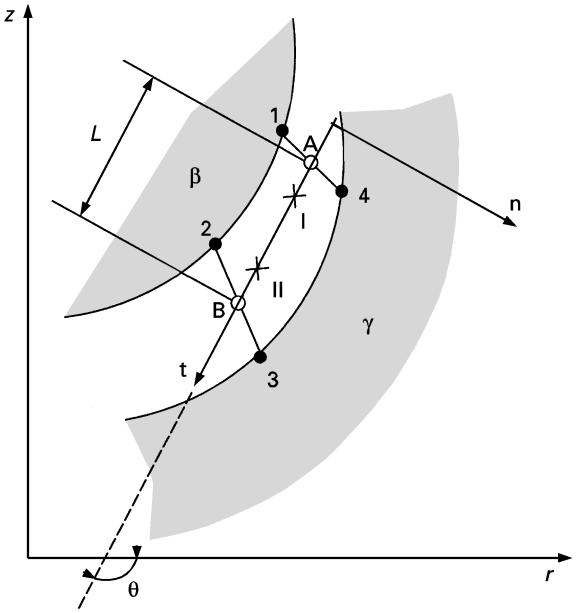


*Figure A1* Definition of the linear, four-node axisymmetric interface element. Nodes 1 and 4 and nodes 2 and 3 coincide in the equilibrium (reference) configuration. Internal nodes A and B located at the midpoints of segments connected corresponding nodes in the β and γ sides of the interface, two integration points marked as + and a local t–n co-ordinate system are also indicated.

where $L$ is the A–B element length. The perturbation of interface potential is expressed in terms of the perturbations of the interface displacements at the internal nodes A and B, $U_{\mathrm{t}}^{\mathrm{A}}$, $U_{\mathrm{t}}^{\mathrm{B}}$, $U_{\mathrm{n}}^{\mathrm{A}}$ and $U_{\mathrm{n}}^{\mathrm{B}}$

$$\delta\Phi = \frac{\partial\Phi[U_{\mathrm{t}}(\eta),\ U_{\mathrm{n}}(\eta)]}{\partial U_{\mathrm{n}}}[N_{\mathrm{A}}(\eta)\delta U_{\mathrm{n}}^{\mathrm{A}} + N_{\mathrm{B}}(\eta)\delta U_{\mathrm{n}}^{\mathrm{B}}] + \frac{\partial\Phi[U_{\mathrm{t}}(\eta),\ U_{\mathrm{n}}(\eta)]}{\partial U_{\mathrm{t}}}[N_{\mathrm{A}}(\eta)\delta U_{\mathrm{t}}^{\mathrm{A}} + N_{\mathrm{B}}(\eta)\delta U_{\mathrm{t}}^{\mathrm{B}}] \qquad \text{(A8)}$$

By substituting Equation A8 into Equation A7 and by choosing of the $\delta U_I^N$ ($N = \mathrm{A, B}$; $I = \mathrm{t, n}$) perturbations at a time to be unity and the remaining perturbations to be zero, the corresponding $F_I^N$ component of the nodal force can be expressed as

$$F_I^N = \int_{-1}^{1} \frac{\partial\Phi[U_{\mathrm{t}}(\eta),\ U_{\mathrm{n}}(\eta)]}{\partial U_I} N_N(\eta) L\pi r(\eta)\, d\eta \qquad \text{(A9)}$$

Using a straightforward geometrical procedure and imposing the equilibrium condition, the corresponding residual nodal forces $R_r^{\mathrm{i}}$ and $R_z^{\mathrm{i}}$ (i = 1–4) in the global $r$–$z$ co-ordinate system, are defined as

$$\left.\begin{aligned} R_r^1 &= -R_r^4 = F_{\mathrm{t}}^{\mathrm{A}}\cos\theta - F_{\mathrm{n}}^{\mathrm{A}}\sin\theta \\ R_z^1 &= -R_z^4 = F_{\mathrm{t}}^{\mathrm{A}}\sin\theta - F_{\mathrm{n}}^{\mathrm{A}}\cos\theta \\ R_r^2 &= -R_r^3 = F_{\mathrm{t}}^{\mathrm{B}}\cos\theta - F_{\mathrm{n}}^{B}\sin\theta \\ R_z^2 &= -R_z^3 = F_{\mathrm{t}}^{\mathrm{B}}\sin\theta - F_{\mathrm{n}}^{\mathrm{B}}\cos\theta \end{aligned}\right\} \qquad \text{(A10)}$$

The components of the Jacobian element are next defined as

$$\frac{\partial R_{\mathrm{j}}^{\mathrm{i}}}{\partial U_I^{\mathrm{k}}} = \sum_{I=\mathrm{n,t}} \sum_{N=\mathrm{A,B}} \sum_{\mathrm{j=n,t}} \sum_{M=\mathrm{A,B}} \frac{\partial R_{\mathrm{j}}^{\mathrm{i}}}{\partial F_I^N} \frac{\partial F_I^N}{\partial U_J^M} \frac{\partial U_J^M}{\partial U_I^{\mathrm{k}}} \qquad \text{(A11)}$$

where the components of the internal Jacobian $\partial F_i^N/\partial U_j^M$ (i, j = n, t; N, M = A, B) are calculated by differentiation of Equation (A9). The residual nodal forces given by Equation A10 and the element Jacobian given by Equation A11 are computed in the UEL subroutine, and passed to ABAQUS for the use in its global Newton scheme for accurate assessment of kinematics.

## References


1. S. C. HUANG and E. L. HALL, *MRS Symp. Proc.* **133** (1989) 693.
2. H. E. DEVE and A. G. EVANS, *Acta Metall. Mater.* **39** (1991) 171.
3. K. C. CHAN and Y.-W. KIM, *Metall. Trans.* **22A** (1991) 2021.
4. M. GRUJICIC and P. DANG, *Mater. Sci. Engng* **A224** (1997) 187.
5. V. F. ZACKAY, E. R. PARKER, D. FAHR and R. BUSCH, *Trans. ASM* **60** (1967) 252.
6. G. N. HAIDEMENOPOULOS, PhD thesis, MIT, Cambridge, MA (1988).
7. A. G. EVANS and R. M. CANNON, *Acta Metall.* **14** (1986) 761.
8. M. GRUJICIC and C. P. NARAYAN, *Mater. Sci. Engng* **A151** (1992) 217.
9. *Idem*, *ibid.* **A151** (1992) 227.
10. A. G. EVANS and R. M. McMEEKING, *Acta Metall.* **34** (1986) 2435.
11. M. GRUJICIC and S. G. LAI, *J. Mater. Sci.*, in press.
12. M. S. DAW and M. I. BASKES, *Phys. Rev. Lett.* **50** (1983) 1285.
13. *Idem*, *Phys. Rev.* **B29** (1984) 6443.
14. D. FARKAS, Private communication.
15. M. GRUJICIC and P. DANG, *Mater. Sci. Engng* **A205** (1996) 139.
16. E. S. MACHLIN, *Acta Metall.* **22** (1974) 95.
17. B. SUNDMAN, B. J. JANSSON and J. O. ANDERSSON, *Calphad* **9** (1985) 153.
18. R. A. JOHNSON, *Phys. Rev.* **B39** (1989) 12 554.
19. V. TVERGAARD, *Int. J. Fracture* **18** (1982) 237.
20. R. FLETCHER and C. M. REEVES, *Comput. J.* **7** (1964) 149.
21. P. VILLARS and L. D. CALVERT "Pearson's handbook of crystallographic data for intermetallic phases", vol. 2 (eds) (American Society for Metals, Metals Park, OH, 1985).
22. P. DANG and M. GRUJICIC, *J. Mater. Sci.* **32** (1997) 4865.
23. M. GRUJICIC and P. DANG, *J. Mater. Sci.* **32** (1997) 4875.
24. A. NEEDLEMAN, *J. Appl. Mech.* **54** (1987) 525.
25. S. SOCRATE, PhD thesis, MIT, Cambridge, MA (1996).
26. G. BOZZOLO, J. FERRANTE and J. R. SMITH, *Scripta Metall.* **25** (1991) 1927.
27. ABAQUS User's Manual, Version 5.4, Hibbitt, Karlsson and Sorensen, Inc., Providence, RI (1995).
28. M. GRUJICIC and S. G. LAI, Unpublished work.



*Received 6 October 1997*
*and accepted 11 May 1998*